ELECTROMAGNETIC FERRITE TILE ABSORBER

Anechoic chambers have been used for over forty years to simulate different operating environments for a wide range of frequencies (1–3). These chambers provide an accurate and convenient environment for electromagnetic compatibility (EMC) testing and are important cost-effective tools for achieving EMC compliance. To perform tests in anechoic chambers in the 30 MHz to 1000 MHz frequency range, good low-frequency electromagnetic absorbers are needed. Magnetic materials, such as ferrite tile absorbers, offer the type of low-frequency performance needed for EMC testing inside shielded rooms (or chambers).

The first anechoic chambers were constructed in the early 1950s for antenna measurements. These chambers were equipped with bats of loosely spun animal hair coated with carbon. This broadband "hair" absorber was 5.08 cm (2 in) thick and provided −20 dB of reflectivity (20 log [reflected wave/incident wave]) at normal incidence from 2.4 GHz to 10 GHz. Later in the decade, the hair absorber was replaced by a new generation of absorber that offered −40 dB of reflectivity at normal incidence. Unlike the hair absorber, the new absorber was equipped with a shaped or convoluted front surface. Commercially manufactured absorbers emerged in the 1960s and boasted less than −60 dB of reflectivity at normal incidence. This low reflectivity was obtained at high microwave frequencies, however, where the thickness (tip-to-base dimension) of the pyramids was at least several wavelengths.

The multiple reflections between the electrically thick pyramids account for the excellent performance. Because the individual pyramids are relatively large compared with a wavelength, the sides of the pyramids reflect and re-reflect the incident wave many times. Upon each reflection, a portion of the wave is absorbed by the pyramid. Hence, an extremely small portion of the incident wave energy survives the many reflections that occur before it arrives at the solid absorber base located between the pyramids and the metal chamber wall. Then the remaining wave is absorbed further as it travels through the base until it is reflected by the chamber wall. The reflected wave is absorbed as it proceeds through the absorber base and again experiences the multiple reflections between adjacent pyramids before emerging from the plane defined by the pyramid tips.

Semi-anechoic chambers were first used for emission measurements during the 1970s as an alternative to an open area test site (OATS), a ground-plane facility for emission measurements performed from 30 MHz to 1000 MHz. These chambers were equipped with a conducting floor to simulate the large ground plane employed on the OATS. Because it obviously was impractical to construct a chamber with absorbers several wavelengths long at 30 MHz, the early cham-

bers typically were equipped with 0.91 to 1.83 m (3 to 6 ft) thick absorber. Originally intended to be operated at higher frequencies, this absorber restricted the use of these chambers to approximately the 90 MHz to 1000 MHz frequency range (4).

With the promulgation of emission requirements during the late 1970s, absorber manufacturers were confronted with a growing demand for a compact wideband absorber to operate over the entire 30 to 1000 MHz frequency range. The evolution of compact wideband absorbers was catalyzed in the mid 1980s when techniques to calculate and measure its reflectivity were developed. The first computationally efficient, accurate calculation of absorber reflectivity became possible when the method of homogenization was used in a theoretical model (5–7). Soon afterward, the reflectivity of compact, wideband absorbers was measured directly with large test fixtures (8–11).

To achieve small reflectivities over the entire 30 to 1000 MHz frequency range, compact wideband absorbers must use tapered structures (like pyramids or wedges) that not only operate at frequencies where they are electrically thick, but at the frequencies where they are electrically thin. When an incident wave encounters electrically thin absorbers, it does not "see" the fine structure of the pyramids or wedges. Instead, the incident wave behaves as though it encountered a solid medium whose effective conductivity and permittivity vary with the distance into the medium. These effective material properties differ from the conductivity and permittivity of the actual material used to construct the absorber.

An optimized electrically thin absorber provides a transition from the wave impedance of free space to the wave impedance of the absorber base. With the correct carbon loading, most of the incident wave penetrates the tapered structure (pyramids or wedges) and is absorbed as it travels through their solid base. Moreover, the carbon loading can be adjusted further to obtain cancellation between the portion of the incident wave reflected by the tapered structure and the wave that emerges from the absorber after reflection by the metal wall. This cancellation causes an extremely small reflectivity, albeit over a relatively narrow frequency range. In general, the carbon loading selected for electrically thin, tapered structures differs from the loading employed for electrically thick structures (7).

Although it is possible to achieve good low-frequency performance of carbon-loaded, tapered structures, they are physically large and require large metal enclosures to house them. An alternative to these large carbon-loaded, tapered structures is the ferrite-tile absorber. Electrically thin ferrite tiles were developed in Japan during the early 1960s (12–14) as an alternative to urethane pyramids and wedges. Because they have a wave impedance close to the impedance of free space, the tiles allow direct penetration of the incident wave without significant reflection at the air-to-tile interface. Furthermore, the tiles are magnetically lossy absorbing the penetrating wave almost completely as it travels through the tile. Subsequently, the wave is reflected by the metal wall behind the ferrite and travels toward the ferrite/air interface. As with the electrically thin urethane absorber, the thickness of the ferrite can be selected to achieve narrowband cancellation from the portion of the incident wave reflected at the air-to-tile interface and from the wave that emerges from the ferrite tile after reflection by the metal wall.

Recently, thin urethane pyramids or wedges that operate from about 200 MHz to 1000 MHz have been combined with ferrite tiles that are effective from 30 MHz to 600 MHz. The combination of these two absorbers, along with properly chosen dielectric layers, results in an ultracompact wideband "hybrid" absorber that exhibits excellent performance from 30 MHz to 1000 MHz (15,16). These "hybrid" absorbers are discussed in detail in (3).

In this chapter, we discuss the ferrite tile, ferrite grids, and hybrid combinations of urethane and ferrite absorbers typically used in electromagnetic test chambers for the 30 MHz to 1000 MHz frequency range. We present formulas and calculated reflectivities (or reflection coefficients). We also discuss how material properties and reflectivities are measured for the ferrite-tile absorbers.

MODELING FERRITE TILES

The performance of absorbers is determined by comparing the magnitudes of incident and reflected plane waves, where the absorber is assumed to be an infinite plane. One such comparison is the reflection coefficient Γ, defined as

$$\Gamma = \frac{E_r}{E_i} \tag{1}$$

where E_r is the reflected electric field and E_i is the incident electric field. Alternatively, absorber performance is expressed as reflectivity R in decibels as

$$R = 20 \cdot \log_{10}(|\Gamma|) \text{ [dB]} \tag{2}$$

The smaller the value of R in dB, the better the performance of the absorber.

It is very straightforward to model a ferrite tile theoretically with the aid of classical transmission-line equations. The reflectivity of a solid ferrite tile backed by a metal wall is given by

$$\Gamma = \frac{Z_f - \eta}{Z_f + \eta} \tag{3}$$

where η is defined as

$$\eta = \sqrt{\frac{\mu}{\epsilon}} \tag{4}$$

and

$$Z_f = \eta \frac{1 - e^{-2\gamma d}}{1 + e^{-2\gamma d}} \tag{5}$$

where d is the ferrite thickness and γ is the propagation constant defined by

$$\gamma = j\omega\sqrt{\mu\epsilon} \tag{6}$$

In these expressions ϵ and μ are the complex permittivity and permeability of the ferrite tile. While Eq. (3) is for a normal incident plane wave, it can be modified to handle off-normal incidence by incorporating the angular dependence into the

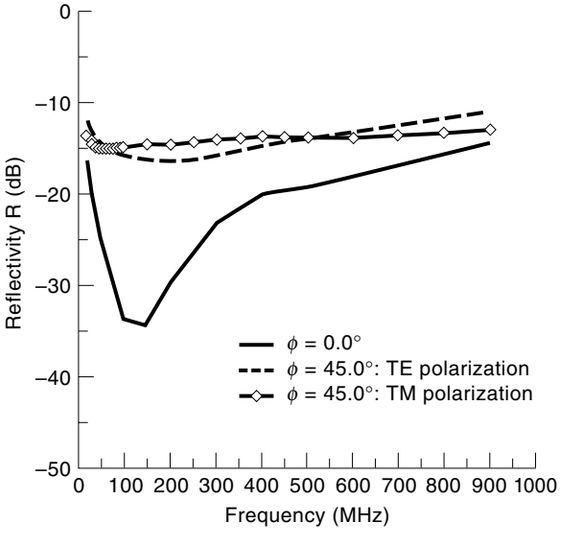

Figure 1. Reflectivity of a 6.38 mm (0.25 in) solid ferrite tile at 0° and 45° incident angles.

impedance and propagation constant [for details, see (3,6,16a)].

Figure 1 shows the reflectivity of a solid ferrite tile and the material properties are given in Table 1. The figure shows that the tile performs very well below 600 MHz, but above 600 MHz, the tile performance deteriorates.

The higher frequency (>600 MHz) performance is improved by using so-called "ferrite grids". A ferrite grid (or waffle) is shown in Fig. 2. The grid is a two-dimensional array of square air sections cut into a ferrite-tile matrix. This structure is modeled with an averaging technique known as homogenization and the transverse material properties are approximated by the following expressions (3):

Table 1. Data on Ferrite Tiles

Frequency (MHz)	Ferrite Tiles			
	Permittivity		Permeability	
	ϵ_r'	ϵ_r''	μ_r'	μ_r''
30	10.88	0.16	52.31	236.17
40	10.93	0.37	31.26	181.36
50	11.04	0.50	21.05	147.02
60	11.24	0.51	15.59	123.51
70	11.39	0.27	12.32	106.32
80	11.41	0.09	9.96	93.56
90	11.37	0.07	8.16	83.57
100	11.19	0.04	6.74	75.52
150	11.29	0.53	3.39	51.64
200	10.97	0.07	1.85	38.77
250	11.37	0.26	1.40	31.38
300	10.93	0.18	0.52	26.23
400	11.00	0.17	0.12	19.82
500	11.03	0.02	0.47	15.66
600	10.95	0.19	0.59	12.93
700	10.99	0.28	0.59	11.07
800	11.18	0.23	0.48	9.69
900	11.31	0.14	0.38	8.55
1000	11.36	0.04	0.29	7.69

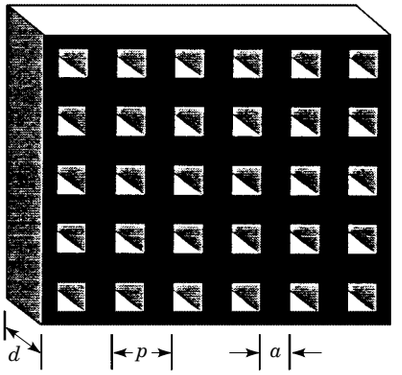

Figure 2. Illustration of the grid or waffle ferrite tile geometry.

$$\epsilon_t = \epsilon_a + \frac{1-g}{\dfrac{1}{\epsilon_0 - \epsilon_a} + \dfrac{g}{2\epsilon_a}}$$

and

$$\mu_t = \mu_a + \frac{1-g}{\dfrac{1}{\mu_0 - \mu_a} + \dfrac{g}{2\mu_a}} \tag{7}$$

The longitudinal permittivity and permeability are known exactly (17) as

$$\epsilon_z = (1-g)\epsilon_0 + g\epsilon_a$$

and

$$\mu_z = (1-g)\mu_0 + g\mu_a \tag{8}$$

In these expressions, $g = a^2/p^2$ is the fraction of space occupied by the absorber, and ϵ_a and μ_a are complex parameters of the bulk ferrite. These material properties then are substituted into Eq. (5) to obtain the reflectivity of the ferrite grid.

The reflectivity of the ferrite grid strongly depends on the filling factor g. One of the advantages of this ferrite grid geometry over the standard solid tile is that there is an additional parameter, the filling factor g, that can be varied to place the nulls (or minimum) of the reflectivity at a desired frequency. The ferrite grid can be designed for wider frequency band performance over that of the standard solid tiles by appropriately choosing the tile thickness, filling factor g, and the material properties of the ferrite. Figure 3 shows results of the reflectivity of a ferrite grid for various values of the filling factor g. The optimum reflectivity of an 18-mm thick ferrite grid with a filling factor of $g = 0.725$ was calculated using the material properties in (18). The results are shown in Figure 4 for normally and obliquely incident waves.

Small, tapered, electric-absorbing structures boast very low reflectivities above about 200 MHz (3), whereas ferrite tiles perform best below 600 MHz. Hence, compact wideband absorbers can be designed by combining tapered electrical absorbers with ferrite tiles. The reflectivity in the 600 MHz to 1000 MHz range is also reduced by simply adding a dielectric

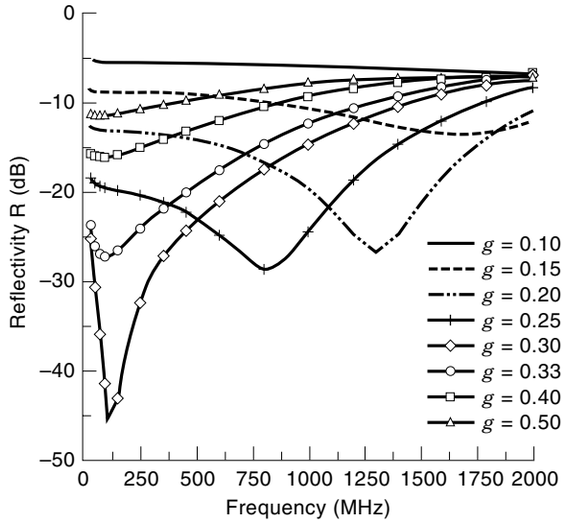

Figure 3. Reflectivity of a 16 mm ferrite grid for various values of the volume fraction g for an incident angle of 0°.

layer between the ferrite and the metal chamber wall. The performance advantages of these so-called "hybrids" are presented in (3).

In the following sections, we discuss how the material properties and the reflectivities of the ferrite tiles are measured.

MEASUREMENTS OF MATERIAL PROPERTIES

Accurate measurements of the high-frequency dispersive magnetic properties of ferrite materials are important for optimally designing a ferrite tile absorber. Magnetic loss mechanisms are strongly frequency-dependent and generally behave nonlinearly. At very low frequencies hysteretic effects (or braking forces acting on Bloch walls in motion) dominantly influence magnetic loss. Eddy currents also produce an *apparent* reduction of permeability and an *apparent* increase of magnetic loss tangent associated with attenuation of the magnetic field inside a ferrite material at low frequencies. However this remains small in most ferrite materials with low dielectric loss.

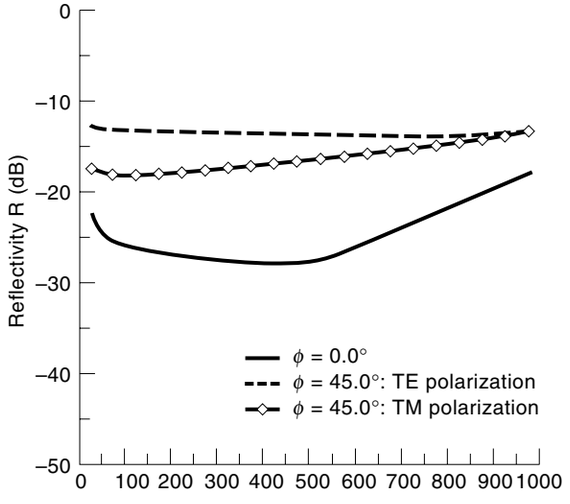

Figure 4. Reflectivity of a ferrite grid at 0° and 45° incident angles for filling factor $g = 0.725$ and a thickness of $d = 18$ mm (0.71 in).

At RF and microwave frequencies, domain wall movement and domain rotation contribute to magnetic loss. The initial permeability spectrum is usually considered to be that part of the permeability spectrum due to domain wall motion. As the RF excitation frequency increases, domain wall rotation no longer fully responds to the excitation. At this point, magnetization does not move in phase with the excitation, and losses occur. Then the real part μ' of the magnetic permeability decreases with increased frequency. The imaginary part, or magnetic loss index μ'', goes through a broad absorptive relaxation.

One characteristic constant of ferrites is the product $f_0 = |\mu_i^*| f_c$, where $\mu_i^* = \mu_i' - j\mu_i''$ is the demagnetized scalar initial permeability and f_c is the corner frequency above which $|\mu_i^*|$ falls off with frequency as $1/f$. For some polycrystalline ferrites, this product represents the frequency at which the relative permeability becomes 1 (19). This rule is only a first-order approximation that depends on the spectral overlap of domain wall and domain rotation relaxation phenomena in the ferrite under test. Another characteristic of ferrite materials is that the peak in the magnetic loss index usually occurs at the frequency where the real permeability has decreased to one-half its static value (20).

Generally, the absorptive window applications of ferrite materials are at frequencies below natural gyromagnetic resonance $\gamma_{gr}M_s$, where M_s is saturation magnetization (T) and γ_{gr} is the gyromagnetic ratio (28 GHz/T or 35.19 MHz · m/kA). At frequencies less than $\gamma_{gr}M_s$, magnetic losses in ferrite materials are high, whereas at frequencies greater than natural gyromagnetic resonance, magnetic losses rapidly decrease. With increasing saturation magnetization, (1) natural gyromagnetic resonance shifts to higher frequencies, (2) f_c increases, and (3) the low-frequency static initial permeability decreases. The absorptive window, similarly, shifts to higher frequencies.

With an applied static magnetic field in the z direction, ferrite materials become uniaxially anisotropic and nonreciprocal, and the magnetic permeability is described by the well-known nondiagonalized tensor

$$\overline{\overline{\mu}} = \mu_0 \begin{bmatrix} \mu^* & j\kappa^* & 0 \\ -j\kappa^* & \mu^* & 0 \\ 0 & 0 & \mu_z^* \end{bmatrix} \tag{9}$$

where $\mu^* = \mu' - j\mu''$ is the principal direction transverse component of the magnetic permeability, $\mu_z^* = \mu_z' - j\mu_z''$ is the parallel component, and $\kappa^* = \kappa' - j\kappa''$ is the off-diagonal transverse component. All components of the magnetic permeability tensor are complex because of ferrite magnetic losses. Particular tensor components depend on ferrite composition, porosity, grain size, saturation magnetization, and RF frequency, temperature, and applied static magnetic field strength. Near ferromagnetic resonance (with an applied static field) saturated ferrite losses are expressed by the resonance line width. Without an applied static field, the ferrite in the demagnetized state is isotropic and reciprocal. In this

case the permeability tensor reduces to the scalar frequency-dependent permeability, $\mu_d^* = \mu_d' - j\mu_d''$.

Regardless of general spectral characteristics, the magnetic properties of ferrite materials must be measured at microwave frequencies. Experimental procedures for accurate magnetic permeability measurements on demagnetized ferrites, therefore, depend spectrally on which side of the natural gyromagnetic resonance the magnetic characterization is desired. At frequencies lower than $\gamma_{gr}M_s$, one-port permeameter and two-port coaxial transmission line measurements provide accurate magnetic permeability characterization of ferrite materials. At microwave frequencies above $\gamma_{gr}M_s$, resonant cavity or dielectric resonator techniques must be used.

Transmission Line Measurement

The goal of this section is to present transmission line measuring methods for permeability (21). In the measurement, a sample is inserted into a waveguide or a coaxial line, and the sample is subjected to an incident electromagnetic field. In developing the scattering equations, usually only the fundamental waveguide mode is assumed to exist. At low frequencies, the impedance of the sample is measured. At microwave frequencies, the two-port scattering matrix is measured. Reflection coefficient and scattering equations are found from an analysis of the magnetic field in the sample holder. Both high- and low-frequency measurements are considered. The first technique, the permeameter, is a low-frequency technique. When lumped circuit parameters (LCR) are used as data, this method is limited to frequencies below 50 MHz. The method is extended to a higher frequency by using reflection coefficient data from a network analyzer. As the operating frequency increases to the point where there is an appreciable electric field in the sample, however, then knowledge of the permittivity is required. The second technique is the transmission line scattering parameter technique. This technique is limited to microwave frequencies, because the measured phase change across the sample becomes inaccurate below 1 MHz. Previous work using the coaxial line for magnetic measurements has been done for example, by Von Hippel (22), Bussey (23), Geyer and Baker–Jarvis (24), and Hoer (25).

Permeameters. The permeameter consists of a short-circuited coaxial sample holder (see Fig. 5) with a sample on the inner conductor of a coaxial line terminated in a short circuit. The advantages of this approach are the ease of sample installation and the broad frequency capability. An air-gap correction is not necessary for permeability measurements because the magnetic field is tangential to air gaps. In this technique, a LCR meter is used to measure admittance Y in the frequency range of 100 Hz to 1 MHz. Then this admittance is converted to a reflection coefficient by $\Gamma = (Y_0 - Y)/(Y_0 + Y)$, where Y_0 is the admittance without the sample. The reflection coefficient for a sample positioned next to a short-circuited termination is given by

$$\Gamma = \exp[-2(\gamma_a L_a + \gamma_t L_t)]\frac{\tanh(\gamma L) - \dfrac{\mu_0\gamma}{\mu\gamma_0}}{\tanh(\gamma L) + \dfrac{\mu_0\gamma}{\mu\gamma_0}} \tag{10}$$

where γ is the propagative constant in the material given by

$$\gamma = j\sqrt{\frac{\omega^2\mu_r^*\epsilon_r^*}{c_{vac}^2} - \left(\frac{2\pi}{\lambda_c}\right)^2} \tag{11}$$

Also, c_{vac} is the speed of light in a vacuum; L is the sample length, the subscripts a and t denote air-line section in the connector and support bead; λ_c is the cutoff wavelength; and ϵ_o and μ_o are the permittivity and permeability of vacuum, respectively. $\epsilon_r^* = \epsilon_r' - j\epsilon_r''$ and $\mu_r^* = \mu_r' - j\mu_r''$ are the complex permittivity and permeability relative to a vacuum, respectively. This equation is useful for both microwave and low-frequency measurements. At low frequencies the permittivity of the sample does not contribute to the determination of permeability. We have shown the frequency limitation for applying the permeameter technique is given by

$$f \ll \frac{c}{4\pi\mu L} \tag{12}$$

where c is the speed of light in a vacuum.

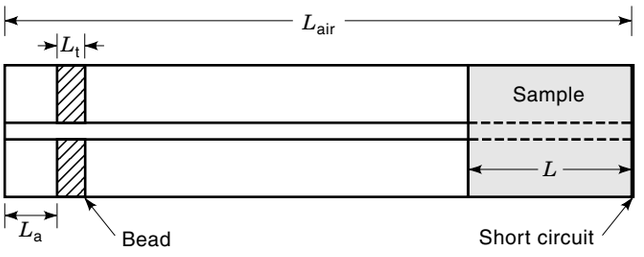

Figure 5. Measurement setup for one-port coaxial line permeameter. Sample resides adjacent to the short circuit.

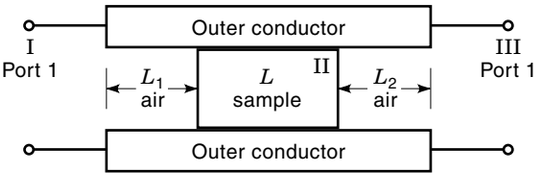

Figure 6. A dielectric sample in a transmission line. Port 1 and Port 2 denote positions of calibration reference planes.

Two-Port Permeability and Permittivity Determination. The two-port scattering parameter technique is used from approximately 50 MHz to microwave frequencies and yields both permittivity and permeability (see Fig. 6). The scattering parameters are defined in terms of the reflection coefficient Γ and the transmission coefficient z by

$$S_{11} = R_1^2\left[\frac{\Gamma(1-z^2)}{1-\Gamma^2 z^2}\right] \tag{13}$$

$$S_{22} = R_2^2\left[\frac{\Gamma(1-z^2)}{1-\Gamma^2 z^2}\right] \tag{14}$$

$$S_{21} = R_1 R_2\left[\frac{z(1-\Gamma^2)}{1-\Gamma^2 z^2}\right] \tag{15}$$

and

$$\gamma_0 = j\sqrt{\left(\frac{\omega}{c_{lab}}\right)^2 - \left(\frac{2\pi}{\lambda_{nc}}\right)^2} \tag{16}$$

where γ_0 is the propagation constant in a vacuum, c_{lab} is the speed of light, and ω is the radian frequency.

$$R_1 = \exp(-\gamma_0 L_1) \tag{17}$$

and

$$R_2 = \exp(-\gamma_0 L_2) \tag{18}$$

are the respective reference plane transformations. Equations (13) through (15) are derived in detail by Hoer and Rasmussen (25). The transmission coefficient z is expressed as

$$z = \exp(-\gamma L) \tag{19}$$

and the reflection coefficient is defined as

$$\Gamma = \frac{\dfrac{\mu}{\gamma} - \dfrac{\mu_0}{\gamma_0}}{\dfrac{\mu}{\gamma} + \dfrac{\mu_0}{\gamma_0}} \tag{20}$$

For a coaxial line, the cutoff frequency approaches 0 ($\omega_c \to 0$).

To obtain both the permittivity and the permeability from the scattering parameter relationships, at least two independent measurements are necessary. In the full scattering parameter solution, a solution of the equations is obtained that is invariant to reference planes for ϵ_r^* and μ_r^*. A set of equations for single-sample magnetic measurements for an air line of length L_{air} is

$$S_{11}S_{22} - S_{21}S_{12} = \exp -2\gamma_0(L_{air} - L)\frac{\Gamma^2 - z^2}{1 - \Gamma^2 z^2} \tag{21}$$

and

$$(S_{21} + S_{12})/2 = \exp -\gamma_0(L_{air} - L)\frac{z(1 - \Gamma^2)}{1 - \Gamma^2 z^2} \tag{22}$$

It is possible to obtain an explicit solution to Eqs. (21) and (22). If $x = (S_{21}S_{12} = S_{11}S_{22})\exp[2\gamma_0(L_{air} - L)]$ and $y = [(S_{21} + S_{12})/2]\exp[\gamma_0(L_{air} - L)]$, then the physical roots for the transmission coefficient are given by

$$Z = \frac{x+1}{2y} \pm \sqrt{\left(\frac{x+1}{2y}\right)^2 - 1} \tag{23}$$

and the reflection coefficient is expressed as

$$\Gamma_2 = \pm\sqrt{\frac{x - Z^2}{xZ^2 - 1}} \tag{24}$$

The ambiguity in the $\pm$ sign in Eq. (24) is resolved by considering the reflection coefficient calculated from S_{11} alone:

$$\Gamma_3 = \frac{\alpha(Z^2 - 1) \pm \sqrt{\alpha^2 Z^4 + 2Z^2(2S_{11} - \alpha^2) + \alpha^2}}{2S_{11}Z^2} \tag{25}$$

where $\alpha = \exp(-2\gamma_0 L_1)$. The correct root for Γ_3 is chosen by requiring that $|\Gamma_3| \leq 1$. An estimate of L_1 is needed in Eq. (25). If Γ_2 is compared with Γ_3, then the $\pm$ sign ambiguity is resolved and therefore Γ_2 is determined. Then the permeability and permittivity are

$$\mu_r^* = -\frac{1 + \Gamma_2}{1 - \Gamma_2}\frac{1}{\gamma_0 L}(\ln Z + 2\pi jn) \tag{26}$$

and

$$\epsilon_r^* = \frac{c^2}{\omega^2}\left[\left(\frac{2\pi}{\lambda_c}\right)^2 - \frac{1}{L^2}(\ln Z + 2\pi jn)^2\right] \Big/ \mu_r^* \tag{27}$$

where $n = 0, \pm 1, \pm 2, \ldots$. The correct value of n is chosen by using a group-delay comparison test. At low frequencies, the correct roots are identified more easily because they are more widely spaced.

Equations (26) and (27) have an infinite number of roots for magnetic materials, because the logarithm of a complex number is multivalued. To choose the correct root, it is necessary to compare the measured group delay with the calculated group delay. The calculated group delay is related to the change of the wave number k with respect to the angular frequency by

$$\tau_{\text{calc.group}} = -L\frac{d}{df}\sqrt{\frac{\epsilon_r^*\mu_r^* f^2}{c^2} - \frac{1}{\lambda_c^2}} \tag{28}$$

$$= -\frac{1}{c^2}\frac{f\epsilon_r^*\mu_r^* + f^2\dfrac{1}{2}\dfrac{d(\epsilon_r^*\mu_r^*)}{df}}{\sqrt{\dfrac{\epsilon_r^*\mu_r^* f^2}{c^2} - \dfrac{1}{\lambda_c^2}}}L \tag{29}$$

The measured group delay is given by

$$\tau_{\text{meas.group}} = \frac{1}{2\pi}\frac{d\phi}{df} \tag{30}$$

where ϕ is the phase of Z. To determine the correct root, the calculated group delays are found from Eq. (29) for various values of n in the logarithm term, where $\ln Z = \ln |Z| + j(\theta + 2\pi n)$. The calculated and measured group delays are compared to yield the correct value of n. When there is no loss in the sample under test, the solution is divergent at integral multiples of one-half wavelength in the sample. This occurs because the phase of S_{11} cannot be measured accurately for small $|S_{11}|$. In the low loss limit, both of the scattering equations reduce to the relationship $Z^2 \to 1$, which is a relationship only for the phase velocity, and therefore solutions for ϵ_r^* and μ_r^* are not separable. This singular behavior is minimized in cases where permeability is known a priori, as shown in previous work performed by Baker-Jarvis (21).

A measurement on a ferrite material is given in Fig. 7 using both the permeameter and two-port techniques. This figure indicates that the permeameter method breaks down around 50 MHz.

Dielectric-Resonator Measurements

At frequencies above $\gamma_{gr}M_s$, resonant-cavity (26–30) or dielectric-resonator techniques (31–35) must be used to accurately

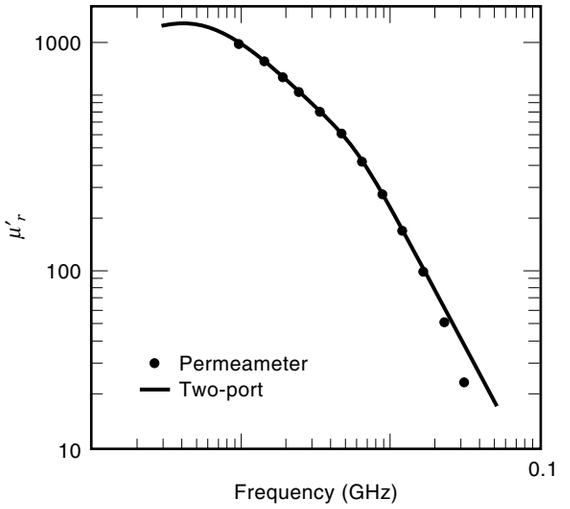

Figure 7. The measured real part of the permeability using both the permeameter and scattering techniques.

characterize ferrite magnetic properties. Commonly used fixtures for determining the demagnetized scalar permeability μ_d^* are either a H_{011} mode cavity for measuring one cylindrical sample or a rectangular cavity operating in the TE_{102} mode with a small spherical sample placed at the center (36). Both of these techniques generally employ perturbation theory, which restricts sample size and, accordingly, allowable magnetic energy partial filling factors and sensitivity to measure small changes in the Q-factor. More recently, Latrach, Le Roux, and Jecko (30) have used a TM_{mn0} cavity for permeability measurements of ferrite disk samples from 2 GHz to 8 GHz. By dielectrically loading the TM_{mn0} cavity, the measured resonant frequency was changed. The method presented here, discussed in more detail in (33–35), uses low-loss H_{011} dielectric resonators, containing the ferrite sample under test, whose complex permittivity is given by $\epsilon_f^* = \epsilon_f' - j\epsilon_f''$. The aspect ratios and permittivities of the dielectric resonators are chosen to spectrally characterize a *single* sample over a broad frequency range. The H_{011} resonant system used in these measurements is illustrated in Fig. 8. The resonators are coupled to the external microwave source through two loop-terminated coaxial cables, and these are adjusted so that the measured loaded Q-factor is equal to the unloaded Q-factor within any prescribed accuracy.

Formulations for the electromagnetic fields in a ferrite rod and in coaxial cylindrical dielectric layers surrounding the rod are found in several papers and textbooks (37–51). At the boundaries between the cylindrical interfaces, the well-known continuity conditions between tangential electric and magnetic field components must be satisfied. At the conductive ground planes, tangential electric fields must vanish. These well-known boundary conditions create a system of linear equations with respect to the constant coefficients in the field expressions, which have nontrivial solutions only if the corresponding determinant vanishes. For fixed values of dimensions and material properties of the resonant system, it is possible to find eigenvalues as roots of the determinant equation. Material properties are determined by measuring resonant frequencies and unloaded Q factors of the dielectric ring resonators with and without the ferrite sample.

The H_{011} resonant frequencies of a ring resonator with a ferrite sample are determined by ϵ_{rr}', ϵ_f', and μ_d', where ϵ_{rr}' is the relative permittivity of the dielectric ring resonator. For ferrite sample diameters less than one-quarter of the external ring resonator diameter, these resonant frequencies are primarily determined by ϵ_{rr}' and μ_d'.

The first step in the measurement process is to verify the complex permittivity of the ferrite sample under test with a TM_{0n0} cavity. Second, the complex permittivities of each dielectric ring resonator are found from measurements of the resonant frequencies and unloaded Q factors of the empty ring resonators operating in the H_{011} mode, given the geometrical dimensions of the resonators and taking into account conductive microwave losses of the upper and lower ground planes. Then values of the imaginary parts of ϵ_f^* and ϵ_r^* are calculated, assuming a linear increase with frequency. Next, the scalar permeability μ_d', computed from measurements of the resonant frequency of these resonators, which contain a completely demagnetized sample and operate in the H_{011} mode, is evaluated from the H_{011} eigenvalue equation in determinant form:

$$F(\epsilon_f', \mu_d', f_0) = 0 \tag{31}$$

where f_0 is the measured resonant frequency of the H_{011} mode for a resonator containing the demagnetized ferrite sample.

After μ_d' is determined, the imaginary part of the permeability, $\mu_f'' = \mu_f' \tan \delta_{m,f}$, is found as a solution to the equation

$$Q^{-1} = Q_c^{-1} + p_{\epsilon_r'} \tan \delta_{e,r} + p_{\epsilon_f'} \tan \delta_{e,f} + p_{\mu_d'} \tan \delta_{m,f} \tag{32}$$

where Q is the unloaded Q factor for the H_{011} mode; Q_c is the Q factor representing conductor losses in the metal plates for the H_{011} mode; $p_{\epsilon_r'}$ is the electric-energy-filling factor for the

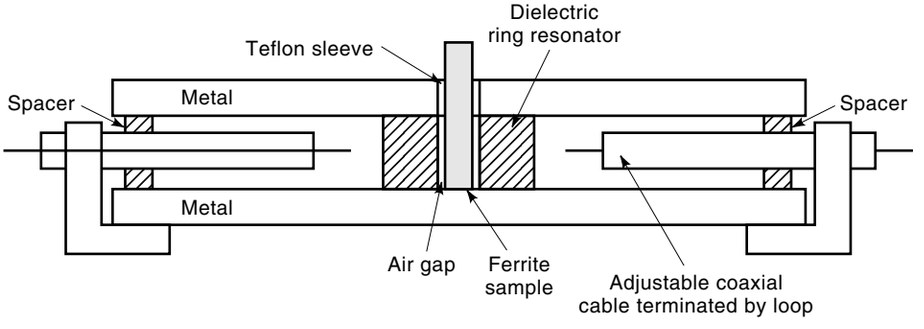

Figure 8. Parallel-plate H_{011} resonant configuration used to measure magnetic permeability.

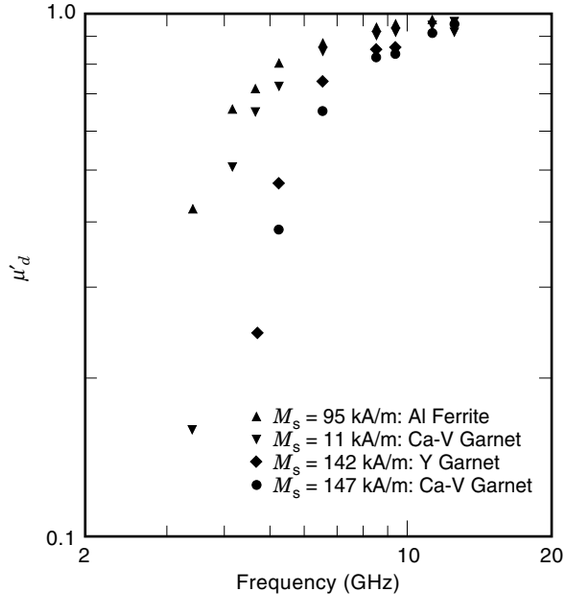

Figure 9. Measured relative permeability μ'_d of several aluminum-doped, calcium-vanadium, and yttrium garnet ferrites with 9 kA/m $\leq M_s \leq$ 147 kA/m as a function of frequency.

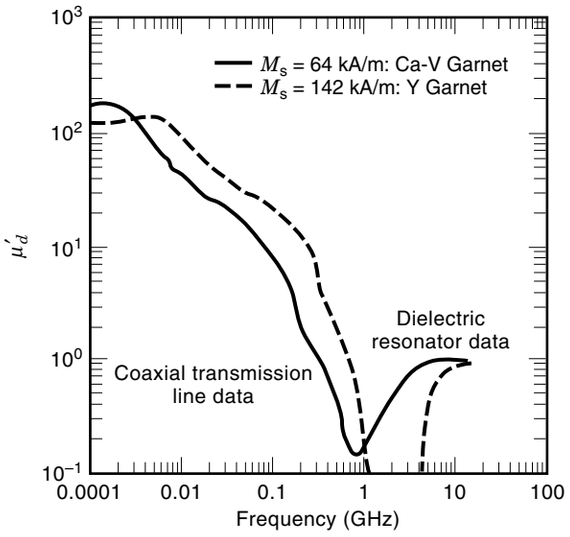

Figure 11. Combined two-port coaxial transmission line and dielectric resonator relative permeability measurements for yttrium and calcium-vanadium garnet ferrites from 1 MHz to 10 GHz.

dielectric ring resonator; $p_{\epsilon_f'}$, $p_{\mu_d'}$ are the ferrite sample electric- and magnetic-energy-filling factors; tan $\delta_{e,r}$ and tan $\delta_{e,f}$ are the dielectric loss tangents of the ring resonator and the ferrite sample under test; and tan $\delta_{m,f}$ is the magnetic loss tangent of the ferrite.

Typical measurement data for bulk ceramic ferrites by this technique are given in Figs. 9 and 10. Uncertainties in μ'_d for typical dimensional uncertainties in the geometric parameters of the dielectric ring resonators and the ferrite sample under test are estimated to be $\pm 0.8\%$, that is, μ''_d is $\pm 1 \times 10^{-5}$. Combined complex permeability data of two ferrites with differing saturation magnetizations over greater than four frequency decades, where both two-port coaxial transmission line and dielectric resonator data have been combined, are shown in Figs. 11 and 12. The rapid increase in magnetic loss, as natural gyromagnetic resonance is approached, is clearly seen. In addition, the large differences in nonlinear magnetic loss behavior over a broad frequency range are apparent.

The total attenuative losses of ferrite-tile absorbers should include both the dielectric and magnetic properties of the ferrite materials under examination. For a plane-wave TEM field, the attenuative loss α is given by

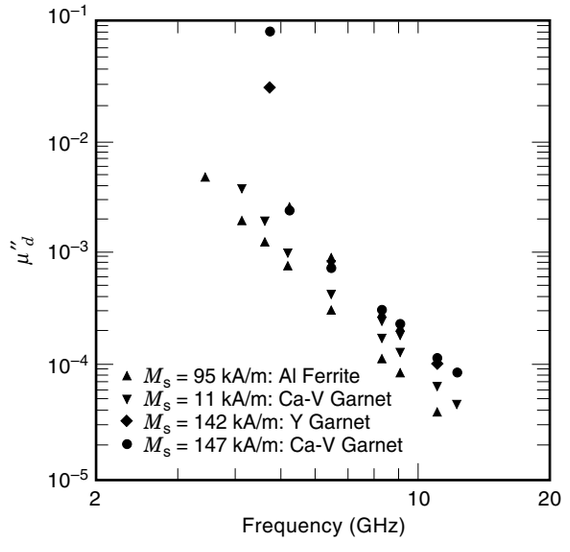

Figure 10. Measured relative magnetic loss index μ''_d of several aluminum-doped, calcium-vanadium, and yttrium garnets with 95 kA/m $\leq M_s \leq$ 147 kA/m as a function of frequency.

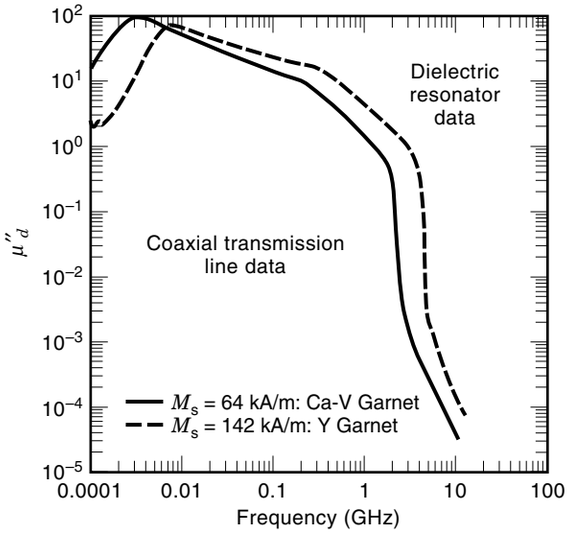

Figure 12. Combined two-port coaxial transmission line and dielectric resonator measurements of relative magnetic loss index for yttrium and calcium-vanadium garnet ferrites from 1 MHz to 10 GHz.

$$\alpha = \frac{\sqrt{2}\omega}{2c} \sqrt{\epsilon'_f \mu'_f [(1+\tan^2 \delta_{e,f})^{1/2}(1+\tan^2 \delta_{m,f})^{1/2} + \tan \delta_{e,f} \tan_{m,f}]} \quad (33)$$

where c is the speed of light.

REFLECTIVITY MEASUREMENTS

In designing a ferrite absorber that performs well over a selected frequency range, it is important to measure the reflectivity of the absorber for normal and oblique incidence. However, the large test fixtures currently used to characterize an absorber from 30 MHz to 1000 MHz allow measuring reflectivities only at normal incidence (8–11). Although an arch is used to measure reflectivities at oblique angles, it is useful only at frequencies above approximately 600 MHz (52,53). An alternative to these techniques is a method under development at the National Institute of Standards and Technology (NIST) in Boulder, CO. This alternative technique uses time-frequency methods to measure reflectivity at arbitrary angles and polarization (54–56).

A block diagram of the bistatic free-space reflectivity measurement system at NIST is depicted in Fig. 13. The measurement system consists of a time- or frequency-domain network analyzer, two TEM horn antennas, and interconnecting RF/microwave cables with a 50 Ω characteristic impedance. More detailed descriptions of time- and frequency-domain versions of this measurement system are given in (54–58). A rectangular ferrite-tile sample (or metal plate reference) is placed in the plane of the two TEM horn antennas at a distance of 1 to 4 m. The level of the sample center is adjusted to match the antenna aperture centers, and the normal to the sample surface bisects the angle between the two horn antenna apertures. The measurements are performed in an ordinary room (laboratory, warehouse, etc.) or in an absorber-lined chamber (semi- or fully anechoic). To minimize the effects of floor, ceiling, and wall reflections, the sample under test should be situated centrally within the room volume.

Obtaining the scattering characteristics of the ferrite tile sample under test requires the following steps:

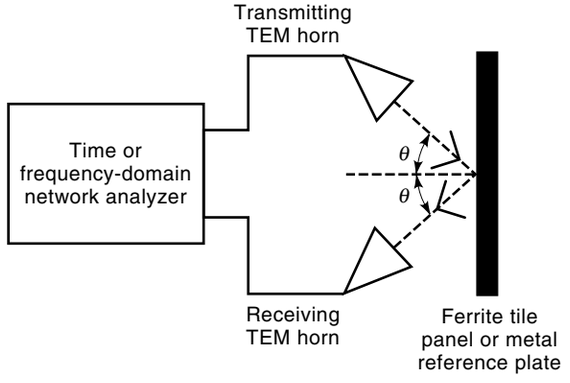

Figure 13. Bistatic free-space RF absorber reflectivity measurement system.

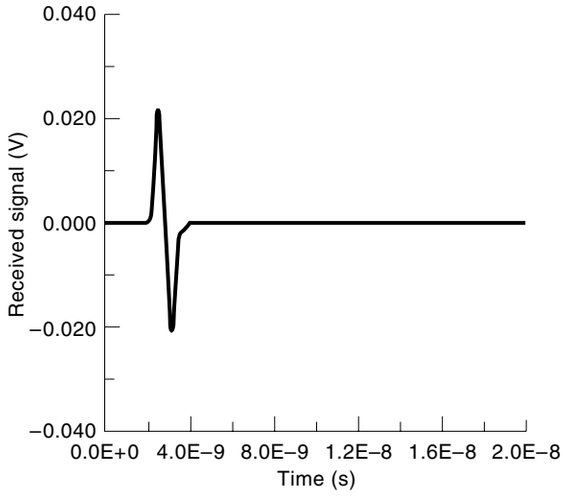

Figure 14. Gated time-domain metal reference plate waveform.

1. A time-domain waveform is obtained for the ferrite-tile sample under test by placing it close to the TEM horn antennas (typically from 1 to 4 m from the antenna apertures).
2. The sample is removed and a background time-domain waveform is obtained.
3. The waveform of step (2) is subtracted from that of step (1). The resulting wave-form consisted of the ferrite-tile sample response plus a component that emanates from the shadow region behind the sample. This process removes significant systematic effects due to antenna-to-antenna coupling and spurious environmental reflections.
4. The shadow-region waveform component is readily eliminated by time-gating, which deletes the undesired waveform component(s). Time-gating works only if there is sufficient separation between the sample and the wall directly behind it, which allows the absorber response to die out before the shadow-region component arrives.
5. Steps (1)–(4) are repeated for a rectangular (or square) metal reference plate. The NIST system employs a 3 m × 3 m metal plate.
6. The time-gated absorber and metal reference plate waveforms obtained in steps (5) and (6) are each Fourier transformed to obtain scattering amplitude spectra.
7. Then the amplitude spectra are divided to obtain the backscatter coefficient which is given by

$$\mathrm{BC}(f,\theta) = \frac{|\mathrm{FT}(\text{gated absorber waveform})|}{|\mathrm{FT}(\text{gated reference waveform})|} \quad (34)$$

where f is the frequency, θ is the angle of incidence, FT denotes the Fourier transform, and BC is the backscatter coefficient. The backscatter coefficient is a real, frequency-domain quantity that directly compares the reflection characteristics of the ferrite-tile absorber system under test with that of the metal plate reference signal. The smaller the backscatter coefficient, the better the performance of the ferrite-tile system.

Examples of gated time-domain reference and ferrite-tile-panel waveforms are shown in Figs. 14 and 15, respectively.

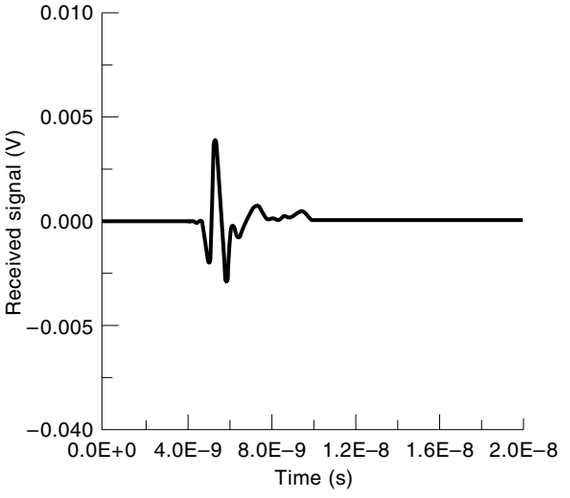

Figure 15. Gated time-domain ferrite-tile waveform.

These waveforms are obtained from a bistatic measurement at a 30° angle of incidence with both the receiving and transmitting antennas horizontally polarized. A synthetic time-domain method is used (58) in which the acquired frequency-domain data are Fourier transformed into time-domain waveforms. The reference waveform of Fig. 14 is obtained from a 3 m × 3 m metal reference plate, located 3.0 m from the antenna aperture centers. It is interesting to note that the reference waveform is nearly a perfect doublet, a result of the differentiating properties of TEM horns in the transmitting mode (59). The corresponding waveform obtained for a 2.4 m × 2.4 m ferrite-tile panel backed by a plywood layer and metallic ground plate is depicted in Fig. 15. Reflections from the front and back surfaces of the ferrite tiles produce the initial triplet (5 ns to 7 ns). Wavefront curvature and finite sample size are responsible for the portion of the waveform that occurs after 7 ns. The frequency-domain backscatter coefficient characteristics from these gated waveforms are depicted in Fig. 16 for a frequency range of 3 MHz to 500 MHz. The characteristic notch that occurs slightly above 300 MHz is a phenomenon typical for ferrite tile systems backed by a ground plane.

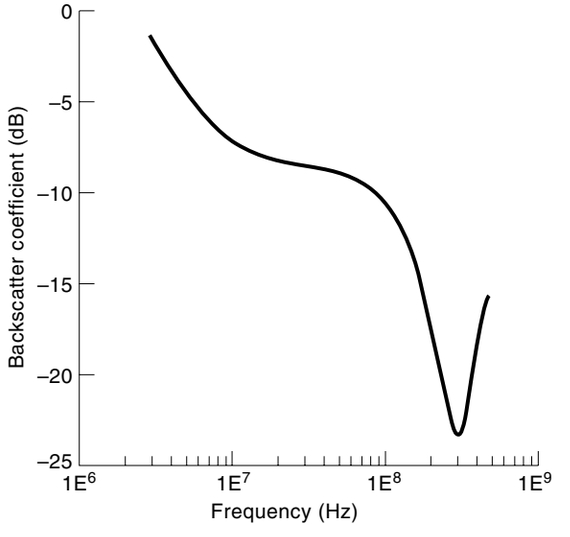

Figure 16. Backscatter coefficient results obtained from the waveforms of Figs. 14 and 15 in conjunction with Eq. (34).

CONCLUSION

In this article, ferrite tile electromagnetic absorbing materials were discussed. Methods to model performance, measure material properties, and measure the reflectivity of this type of absorbing material were presented. The advantages of the ferrite-tile absorber are that they are small and offer very low reflectivity in the frequency range of 30 MHz to 600 MHz. However, above 600 MHz the performance of these ferrite tiles begins to degrade. Dielectric layers behind the ferrite tiles and tapered electric absorbing structures in front of the tiles are used to improve the high-frequency performance of the ferrites. A discussion on how well these hybrid absorbers work is found in (3). The next generation of ferrite-tile absorbers, consisting of thin magnetic layers (60–63) and a combination of ferrite layers with chiral materials (3), is currently being developed.

BIBLIOGRAPHY

1. A. J. Simmons and W. H. Emerson, An anechoic chamber making use of a new broadband material. *Convention Record of the IRE 1953 National Convention: Part 2-Antennas and Communications,* pp. 31–41.
2. W. H. Emerson, Electromagnetic wave absorbers and anechoic chambers through the years. *IEEE Trans. Antennas Propagat.,* **21**: 484–490, 1973.
3. C. L. Holloway et al., Comparison of electromagnetic absorber used in anechoic and semi-anechoic chambers for emissions and immunity testing of digital devices. *IEEE Trans. Electromag. Compat.,* **39**: 33–47, 1997.
4. R. F. German, Comparison of semi-anechoic chambers and open-field site attenuation measurements. *Proc. 1982 IEEE International Symposium on Electromagnetic Compatibility,* Santa Clara, CA, September 8–10, 1982, pp. 260–265.
5. E. F. Kuester and C. L. Holloway, Improved low-frequency performance of pyramid-cone absorbers for application in semi-anechoic chambers, *Proc. 1989 IEEE National Symposium on Electromagnetic Compatibility,* Denver, CO, May 23–25, 1989, pp. 394–399.
6. E. F. Kuester and C. L. Holloway, A low-frequency model for wedge or pyramid absorber arrays-I: theory, *IEEE Trans. Electromagn. Compat.,* **36**: 300–306, 1994.
7. C. L. Holloway and E. F. Kuester, A low-frequency model for wedge or pyramid absorber arrays-II: computed and measured results, *IEEE Trans. Electromagn. Compat.,* **36**: 307–313, 1994.
8. N. Ari, D. Hansen, and H. Garbe, Analysis and measurements of electromagnetic scattering by pyramidal absorbers, *8th Int. Zurich Symp. Technical Exhibition Electromagnetic Compatibility,* Zurich, March 7–9, 1989, pp. 301–304.
9. D. Hansen, N. Ari, and H. Garbe, An investigation into the scattering and radiation characteristic of RF-absorbers, *Proc. 1988 IEEE International Symposium on Electromagnetic Compatibility,* Seattle, WA, August 2–4, 1988), pp. 99–105.
10. S. Takeya and K. Shimada, New measurement method of RF absorber characteristics by large square coaxial line. *Proc. 1988 IEEE International Symposium on Electromagnetic Compatibility,* Dallas, TX, August 9–13, 1993, pp. 397–402.

11. P. Pues, Electromagnetic wave absorber measurement in a large coax, *9th Int. Zurich Symp. Technical Exhibition Electromagnetic Compatibility,* Zurich, March 1991, pp. 541–546.
12. Y. Naito et al., Characteristics of the ferrite absorbing wall, *Trans. I.E.C.E., Japan,* **52-B** (1): 26, 1969 (available in English in *Electronics and Communication in Japan,* p. 76, 1969).
13. Y. Natio and E. Fujiwara, Thickness of electromagnetic wave absorber utilizing ferrite, *Trans. I.E.C.E., Japan,* **53-B** (9): 537, 1970 (available in English in Electronics and Communication in Japan, p. 94, 1970).
14. Y. Natio, On the permeability dispersion of a spinel ferrite, *Electronics and Communication in Japan,* **56-C** (2): 118–123, 1973.
15. T. Ellam, An update on the design and synthesis of compact absorber for EMC chamber applications, *Proc. 1994 IEEE International Symposium on Electromagnetic Compatibility,* Chicago, August 22–26, 1994, pp. 408–412.
16. K. Ishino et al., Realization of compact semi- and fully anechoic chambers using a new developed composite absorber, *Proc. 1994 IEEE International Symposium on Electromagnetic Compatibility, Chicago,* August 22–26, 1994, pp. 413–418.

16a. L. M. Brekhovskikh, *Waves in Layered Media,* New York: Academic Press, 1960, ch. 1.

17. E. F. Kuester and C. L. Holloway, Comparison of approximations for effective parameters of artificial dielectrics, *IEEE Trans. Microwave Theory Techn.,* **38** (11): 1752–1755, 1990.
18. M. Takahashi, *A new structure of electromagnetic wave absorber,* Toyo Corporation, Technical Report, October 1991.
19. R. G. Geyer et al., Spectral characterization of ferrites for use as magnetic reference materials, *Conf. Precision Electromag. Meas. Dig.,* 1992, pp. 107–108.
20. J. L. Snoek, Dispersion and absorption in magnetic ferrites at frequencies above one Mc/s. *Physica XIV,* **4**: 207–217, 1948.
21. J. Baker–Jarvis et al., Transmission/reflection and short-circuit line methods for measuring permittivity and permeability, Natl. Inst. Stand. Technol., Tech. Note 1355, May, 1992.
22. A. R. V. Hippel, *Dielectric Materials and Applications,* Cambridge, MA: M.I.T. Press, 1954.
23. R. B. Goldfarb and H. E. Bussey, Method for measuring complex permeability at radio frequencies, *Rev. Sci. Instrum.,* **58** (4): 624–627, 1987.
24. R. G. Geyer and J. Baker–Jarvis, Spectral characterization of ferrites for use as magnetic reference materials. *CPEM'92 Digest,* Conference on Precision Electromagnetic Measurements, 1992, pp. 107–108.
25. C. A. Hoer and A. L. Rasmussen, Equations for the radiofrequency magnetic permeameter, *NBS Journal of Research,* **67C**: 69–76, 1963.
26. R. C. LeCraw and E. G. Spencer, Tensor permeabilities of ferrites below magnetic saturation, *IRE Conv. Rec.* New York, pt. 5, 1956, pp. 66–74.
27. J. J. Green and T. Kohane, Testing of ferrite materials for microwave applications, *Semicond. Prod. Solid State Technol.,* **7**: 46–54, 1964.
28. H. E. Bussey and L. A. Steinert, Exact solution for a gyromagnetic sample and measurements on a ferrite, *IRE Trans. Microwave Theory Tech.,* **6**: 72–76, 1958.
29. W. Muller–Gronau and I. Wolff, A microwave method for the determination of the real parts of the magnetic and dielectric material parameters of premagnetized microwave ferrites. *IEEE Trans. Microwave Theory Tech.,* **32**: 377–382, 1983.
30. M. Latrach, P. LeRoux, and F. Jecko, Accurate method for experimental determination of real part of initial permeability of demagnetized ferrite samples. In *Proc. 10eme Colloque Optique Hertzienne et Dielectriques,* Rennes, September 6–8, 1989, pp. 339–342.
31. N. Ogasawara et al., Highly sensitive procedures for measuring permeabilities ($\mu_{\pm}$) for circularly polarized fields in microwave ferrites. *IEEE Trans. Magnetics,* **12**: 256–269, 1976.
32. J. Krupka, Resonant modes in shielded cylindrical ferrite and single crystal resonators. *IEEE Trans. Microwave Theory Tech.,* **37**: 691–697, 1989.
33. R. G. Geyer and J. Krupka, Microwave behavior of ferrites: theory and experiment. *Conf. Digest on Precision Electromagnetic Measurements,* June 17–20, 1996, pp. 206–207.
34. R. G. Geyer and J. Krupka, Complex permeability measurements of microwave ferrites. In *Microwave Processing of Materials V, Materials Research Society Symposium Proceedings,* **430**: 257–262, 1996.
35. J. Krupka and R. G. Geyer, Complex permeability of demagnetized microwave ferrites near and above gyromagnetic resonance *IEEE Trans. Magnetics,* **32** (3): 1924–1933, 1996.
36. J. J. Green and F. Sandy, Microwave characterization of partially magnetized ferrites. *IEEE Trans. Microwave Theory Tech.,* **22**: 641–645, 1974.
37. M. L. Kales, Modes in waveguides containing ferrites, *J. Appl. Phys.,* **24**: 604–608, 1953.
38. H. Suhl and L. R. Walker, Topics in guided wave propagation through gyromagnetic media. Pt. I-The completely filled cylindrical guide, *Bell Syst. Tech. J.,* **33**: 579–659, 1954.
39. E. Snitzer, Cylindrical dielectric waveguide modes. *J. Opt. Soc. Amer.,* **51**: 491–498, 1961.
40. R. A. Waldron, Electromagnetic wave propagation in cylindrical waveguides containing gyromagnetic media, *J. Brit. IRE,* **18**: 597–612, 677–690, and 733–746, 1958.
41. R. A. Waldron, Theory of the mode spectra of cylindrical waveguides containing gyromagnetic media. *J. Brit. IRE,* **19**: pp. 347–356, 1959.
42. R. A. Waldron, Features of cylindrical waveguides containing gyromagnetic media. *J. Brit IRE,* 695–706, 1960.
43. R. A. Waldron, Loss properties of ferrite-loaded cylindrical waveguides containing gyromagnetic media. *J. Brit. IRE,* 321–334, 1963.
44. R. A. Waldron, Properties of ferrite-loaded cylindrical waveguides in the neighborhood of cutoff. *Proc. IEEE,* **109B** (suppl. no. 21): 90–94, 1962.
45. R. A. Waldron, Properties of inhomogeneous cylindrical waveguides in the neighborhood of cutoff, *J. Brit. IRE,* **25**: 547–555, 1963.
46. J. E. Tompkins, Energy distribution in partially ferrite-filled waveguides, *J. Appl. Phys.,* **29**: 399–400, 1958.
47. R. A. Waldron, *Ferrites,* New York: Van Nostrand, 1961.
48. P. J. B. Clarricoats, *Microwave Ferrites,* London: Chapman and Hall, 1961.
49. A. J. Baden–Fuller, *Ferrites at Microwave Frequencies,* London: Peter Peregrinus, 1987, Chap. 3.
50. H. D. Godtmann and W. Hass, Magnetodynamic modes in axially magnetized rods between two parallel conducting sheets. *IEEE Trans. Microwave Theory Tech.,* **15**: 478–480, 1967.
51. A. M. Duputz and A. C. Priou, Computer analysis of microwave propagation in a ferrite circular waveguide-optimization of phase-shifter longitudinal field section, *IEEE Trans. Microwave Theory Tech.,* **22**: 601–613, 1974.
52. E. F. Knott, J. F. Shaeffer, and M. T. Tuley, *Radar Cross Section: Its Prediction, Measurement and Reduction,* Dedham, MA: Artech House, Inc., 1985, Chap. 10.
53. R. E. Hiatt, E. F. Knott, and T. B. A. Senior, *A study of VHF absorber and anechoic rooms,* College of Engineering, Department

of Electrical and Computer Engineering, Radiation Laboratory, University of Michigan, Ann Arbor, Michigan, Tech. Report No. 5391-1-F, February, 1963.

54. S. Tofani, A. Ondrejka, and M. Kanda, Time-domain method for characterizing the reflectivity of absorbing materials from 30 to 1000 MHz, *IEEE Trans. Electromagn. Compat.,* **33**: 234–240, 1991.
55. S. Tofani et al., Bistatic scattering of absorbing materials from 30 to 1000 MHz, *IEEE Trans. Electromagn. Compat.,* **34**: 304–307, 1992.
56. R. Johnk et al., Time-domain measurements of the electromagnetic backscatter of pyramidal absorbers and metallic plates, *IEEE Trans. Electromagn. Compat.,* **35**: 429–433, 1993.
57. R. T. Johnk and A. R. Ondrejka, Electrical material properties from a freespace time-domain RF absorber reflectivity measurement system, *Proc. 1997 IEEE International Symposium on Electromagnetic Compatability,* August 11–22, 1997, Austin, TX.
58. IEEE standard PAR-1128, Recommended practice for RF absorber evaluation, to be published.
59. R. A. Lawton and A. R. Ondrejka, Antennas and the associated time-domain range for the measurement of impulsive fields, Nat. Bur. Stand. (U.S.) Tech. Note 1008, 1978.
60. H. W. Helberg and V. Kose, Die breitbandige absorption electromagnetischer wellen durch dunne ferritschichten, *Zeitschrift für Angewandte Physik,* **19**, 509–514, 1965.
61. F. Mayer and J. P. Chaumat, Dielectromagnetic materials for absorber-lined chambers (ALC). *Proc. 9th International Zurich Symposium on Electromagnetic Compatibility* (Zurich, March 12–14, 1991, pp. 569–572.
62. H. Komori and Y. Konishi, Wideband electromagnetic wave absorber with thin magnetic layers, *IEEE Trans. Broadcasting,* **40**: 219–222, 1994.
63. Z. Cohn, J. Daly, and C. Parker, Advanced ferrite materials for anechoic chambers. *Ceramics Trans.,* **47**: 269–284, 1995.

CHRISTOPHER L. HOLLOWAY
JAMES R. BAKER–JARVIS
ROBERT T. JOHNK
RICHARD G. GEYER
U.S. Department of Commerce,
Boulder Laboratories